

Article

Zero-Voltage Ride-Through Scheme of PMSG Wind Power System Based on NLESO and GFTSMC

Zhongjian Kang and Jinfeng Li * 

College of New Energy, China University of Petroleum (East China), Qingdao 266580, China; kangzjzh@163.com

* Correspondence: z21150106@s.upc.edu.cn

Abstract: In this paper, a scheme for zero-voltage ride through of a permanent magnet synchronous generator wind power system is proposed. Maintaining the stability of DC-link voltage is the key to realizing zero-voltage ride through. A braking chopper is used to dissipate the active power to restrain the rise of DC-link voltage during a grid fault. However, the braking chopper-caused disturbance to the double closed-loop control of the grid side converter makes the control effect on DC-link voltage worse. Therefore, a robust current feedforward control, based on a nonlinear extended state observer and global fast terminal sliding mode control is proposed. A nonlinear extended state observer estimates the total disturbance in the system and compensates for the control law. Global fast terminal sliding mode control enables the system to reach the sliding mode surface in a finite time, and its control law is continuous without switching terms, thereby eliminating the chattering phenomenon. A nonlinear extended state observer and global fast terminal sliding mode control change the current feedforward control into a nonlinear robust current feedforward control. The control effect is improved, and the use of current transformers is reduced in practical applications, thereby reducing costs. The validity of this scheme has been verified by simulation.

Keywords: current feedforward control; global fast terminal sliding mode control; nonlinear extended state observer; permanent magnet synchronous generator; zero voltage ride through



Citation: Kang, Z.; Li, J. Zero-Voltage Ride-Through Scheme of PMSG Wind Power System Based on NLESO and GFTSMC. *Electronics* **2023**, *12*, 4348. <https://doi.org/10.3390/electronics12204348>

Academic Editor: Ahmed Abu-Siada

Received: 15 August 2023

Revised: 23 September 2023

Accepted: 25 September 2023

Published: 20 October 2023



Copyright: © 2023 by the authors. Licensee MDPI, Basel, Switzerland. This article is an open access article distributed under the terms and conditions of the Creative Commons Attribution (CC BY) license (<https://creativecommons.org/licenses/by/4.0/>).

1. Introduction

Among all kinds of renewable energy sources, wind power is one of the fastest-growing [1]. Currently, there are primarily two types of wind-driven generator, namely doubly fed induction generators (DFIGs) and permanent magnet synchronous generator (PMSGs). The high initial installation cost of PMSGs is a drawback. The absence of a gearbox is an advantage. Additionally, the motor side and grid side of PMSG wind power systems are completely decoupled, which makes them susceptible to grid faults [2]. Therefore, in PMSG wind power systems, it is easier to realize zero voltage ride through (ZVRT). PMSG wind power systems are gradually becoming a mainstream technology. With the increase in the penetration rate of wind power generation, the grid codes of wind turbines are particularly significant [3]. Stricter grid codes must be formulated to maintain the existing reliability and stability of grids. Low voltage ride through (LVRT) is one of the most important issues in grid codes, requiring that when the grid voltage sags, the wind turbines keep running without being disconnected from the grid [4]. ZVRT can be considered to be an extreme case of LVRT [5]. It requires that the wind turbine continue operating when the grid voltage drops to zero, which puts further requirements on the fault ride through capability of the wind power system [6]. Many countries have incorporated the requirements of ZVRT into their grid codes.

In the case of a grid fault, the voltage sag of the point of common coupling (PCC) makes the grid side converter (GSC) unable to transmit energy to the grid, resulting in a rise in DC-link voltage and equipment damage. Therefore, it is necessary to install hardware devices or improve the control strategy of the converter to maintain the stability

of DC-link voltage. In addition, the GSC should send reactive power to the grid to help restore grid voltage. Many schemes have been proposed for the LVRT of PMSG wind power systems, including adding hardware devices, improving the control strategy of the full-rated converter, and pitch angle control [2,7]. To implement ZVRT, these measures can also be utilized as a guide.

For the method of adding hardware devices, the most common hardware devices include braking choppers, energy storage systems (ESSs), and flexible alternating current transmission systems (FACTS) [8]. The literature [9] compares different traditional control methods for BCs. BCs have the advantages of a simple control method and low cost. However, they have high requirements for the thermal performance of braking resistance and cause energy waste. Energy storage systems such as battery energy storage system [10], superconducting magnetic energy storage systems [11], and super capacitor energy storage systems [12] have also been applied in LVRT. Compared to BC, these ESSs can efficiently store energy and send it to the grid after the fault. But they have higher costs and more complex control methods. FACTS, such as a dynamic voltage restorer (DVR) [13,14], static var compensator (SVC), and static synchronous compensator (STATCOM) [15], can provide reactive power to the grid to help restore grid voltage. However, they also have drawbacks such as high cost and complex control methods.

For the method of improving the control strategy of a full-rated converter, the main purpose is to limit the active power and supply reactive power to the grid. The motor side converter (MSC) can reduce the unbalanced power between the MSC and the GSC by reducing the active power output. The power difference between the MSC and the generator will accelerate the rotation of the generator rotor in the form of kinetic energy, namely rotor energy storage. However, once the rotor speed exceeds the limit value, the wind turbine will be tripped off from the grid [8,16]. The GSC can switch to STATCOM mode, which prioritizes the output of reactive power to the grid and reduces active power output. This is equivalent to providing reactive power compensation to the system, which helps the recovery of grid voltage. Adding advanced controls such as predictive control [17], virtual synchronous generator (VSG) control and robust adaptive control [18] to the converter control can stabilize the DC-link voltage better.

Pitch angle control reduces the capture of wind energy by adjusting the pitch angle of the wind turbine, thereby reducing power imbalance. The disadvantage of it is the slow response to grid voltage sags because its time scale is much larger than that of the electromagnetic transient part. It is generally used in conjunction with other control strategies such as STATCOM [4], field-weakening control [13], and BCs [19].

The above research focuses on LVRT of PMSG wind power systems. However, there is limited research on ZVRT. These can be used as references for ZVRT. In previous studies, a BC was often used together with rotor energy storage, but its influence on the control effect of DC-link voltage was not considered [20,21]. However, when the grid voltage drops to zero, the power difference between the generator side and the grid side reaches its maximum value. More energy needs to be released by the BC. The switching frequency of the BC is greatly increased. Therefore, a BC has a more significant influence on DC-link voltage control.

In this paper, a BC is used to dissipate the surplus power when the grid experiences a fault. However, the BC causes disturbances to the system and affects the control of the proportional integral (PI) controller over the DC-link voltage, leading to significant voltage fluctuations. Therefore, a current feedforward control based on a nonlinear extended state observer (NLESO) and global fast terminal sliding mode control (GFTSMC) is added to the double closed-loop control of the GSC to suppress voltage fluctuations. An NLESO accurately estimates the system state and estimates the uncertainty of the model and external disturbances. Sliding mode control (SMC) has the characteristics of high accuracy, fast response, and a low requirement for model accuracy [22,23]. Terminal sliding mode control (TSMC) introduces a nonlinear function into the design of the sliding mode surface. This allows the tracking error on the sliding mode surface to converge to zero in a finite

time. GFTSMC combines the advantages of traditional SMC and TSMC in the design of the sliding mode surface, ensuring that the system reaches the sliding mode surface within a limited time. The control law of GFTSMC is continuous, which eliminates the chattering phenomenon. The main contributions of this paper are as follows:

1. A nonlinear robust current feedforward control based on an NLESO and GFTSMC is proposed;
2. A ZVRT scheme for PMSG based on a BC and nonlinear robust current feedforward control is proposed;
3. A comparison with conventional double closed-loop control is made to show the validity of the proposed nonlinear robust current feedforward control and ZVRT scheme.

The structure of this paper is as follows. Section 2 provides a brief description of a PMSG wind power system. In Section 3, the conventional control strategy of PMSG wind power systems is introduced. In Section 4, the nonlinear robust current feedforward control is proposed. In Section 5, a simulation model is established in DigSILENT to verify the validity of the proposed scheme. In Section 6, conclusions are drawn.

2. Basic Description of PMSG Wind Power Systems

The topology of PMSG wind power systems is shown in Figure 1a. It mainly consists of four parts:

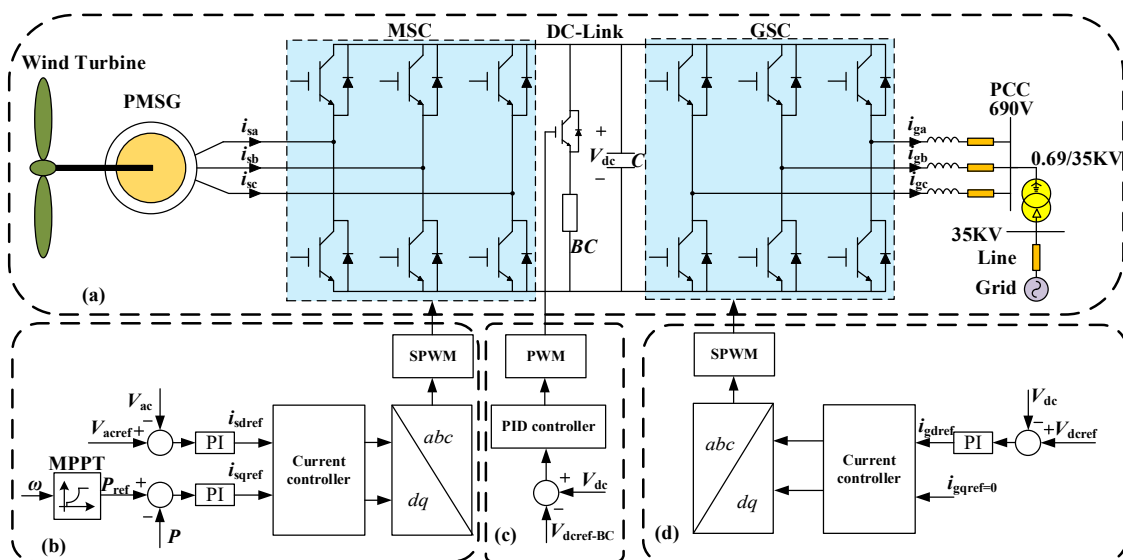


Figure 1. (a) Topology of a PMSG wind power system; (b) control block diagram of the MSC; (c) control block diagram of the BC; (d) control block diagram of the GSC.

1. A wind turbine converts wind energy into mechanical energy. The mechanical power output [24,25] of the wind turbine is given by Equation (1):

$$P_t = 0.5\rho A_{tur} C_p(\lambda, \beta) v_w^3 \tag{1}$$

where, P_t is the output power of the wind turbine, ρ is the air density, A_{tur} is the area swept by the blades, C_p is the power utilization coefficient, λ is tip speed ratio, β is pitch angle, and v_w is wind speed.

The expression of the tip speed ratio is given by Equation (2):

$$\lambda = \frac{\omega_R R}{v_w} \tag{2}$$

where, ω_R is rotor speed, R is radius of wind turbine.

The power utilization coefficient C_p is given by Equation (3):

$$\begin{cases} C_p(\lambda, \beta) = 0.5176\left(\frac{116}{\lambda_i} - 0.4\beta - 5\right)e^{-\frac{21}{\lambda_i}} + 0.0068\lambda \\ \frac{1}{\lambda_i} = \frac{1}{\lambda + 0.08\beta} - \frac{0.035}{\beta^3 + 1} \end{cases} \quad (3)$$

When the pitch angle is fixed, as the tip speed ratio increases, the power utilization coefficient shows a trend of first increasing and then decreasing.

2. A PMSG converts mechanical energy into electric energy. The voltage equation of a PMSG is given by Equation (4):

$$\begin{cases} u_{sd} = R_s i_{sd} + L_s \frac{di_{sd}}{dt} - \omega L_s i_{sq} \\ u_{sq} = R_s i_{sq} + L_s \frac{di_{sq}}{dt} + \omega L_s i_{sd} + \omega \psi \end{cases} \quad (4)$$

where, u_{sd} and u_{sq} are the stator voltage, i_{sd} and i_{sq} are the stator current in dq frame. R_s and L_s are the stator resistance and the stator inductance of the PMSG, respectively. And ω is the rotor flux electrical speed.

Equation (5) shows the electromagnetic torque of the PMSG [26];

$$T_e = \frac{3}{2} p_n [(L_d - L_q) i_{sd} i_{sq} + \psi_r i_{sq}] \quad (5)$$

where, p_n is the number of pole pairs, L_d and L_q are the stator inductance, ψ_r is the amplitude of the rotor flux linkage.

3. Full-rated converter. It consists of an AC-DC converter (MSC), a DC-AC converter (GSC) and the DC-link. Neglecting the losses of the converter, the power relation of the MSC and GSC is given by Equation (6) [27,28]:

$$C V_{dc} \frac{dV_{dc}}{dt} = P_{gen} - P_{grid} = \Delta P \quad (6)$$

where, C is the capacitance of the parallel capacitor, V_{dc} is the DC-link voltage, P_{gen} is the generator power, P_{grid} is the grid power, ΔP is the power difference between generator and grid.

4. External grid, equivalent to a three-phase AC voltage source. The voltage equation of the external grid is given by Equation (7):

$$\begin{cases} u_{gd} = -R_g i_{gd} + L_g \frac{di_{gd}}{dt} + \omega_f L_g i_{gq} + u_{id} \\ u_{gq} = -R_g i_{gq} + L_g \frac{di_{gq}}{dt} + \omega_f L_g i_{gd} + u_{iq} \end{cases} \quad (7)$$

where, u_{gd} and u_{gq} are the grid voltage, i_{gd} and i_{gq} are the grid current, u_{id} and u_{iq} are the GSC voltage in dq frame. R_g and L_g are the resistance and induction of grid, respectively. And ω_f is the angular frequency of the grid voltage.

If the d-axis of the rotating coordinate system is aligned with the voltage vector of the external grid, the active power and reactive power sent to the grid are given as:

$$\begin{cases} P = \frac{3}{2} u_{gd} i_{gd} \\ Q = \frac{3}{2} u_{gq} i_{gq} \end{cases} \quad (8)$$

Therefore, the active power and reactive power sent to the power grid can be controlled by i_{gd} and i_{gq} , i_{gd} and i_{gq} are also referred to as the active current and reactive current.

During normal operation of the extended grid, P_{gen} is equal to P_{grid} , hence $\Delta P = 0$. From Equation (6), $\frac{dV_{dc}}{dt} = 0$. Therefore, DC-link voltage remains stable. When a grid fault causes voltage sag, the output current of the GSC increases. Due to the capacity limitation of the GSC, the increase in output current is limited. Accordingly, P_{grid} is also limited. However, P_{gen} remains unchanged, which is due to $P_{gen} > P_{grid}$. The surplus energy (ΔP)

will be stored in the DC capacitance, resulting in a rise in DC-link voltage [29]. When the grid voltage drops to zero, the DC-link voltage will rise at the maximum speed. The rise in DC-link voltage causes damage to power electronic devices, and even affects the safety of the entire power generation system. It ultimately leads to the failure of ZVRT. Thus, limiting the power imbalance and maintaining the stability of DC-link voltage are the primary challenges of ZVRT of PMSG wind power systems.

3. Conventional Control Strategy of PMSG Wind Power Systems

3.1. MSC Control

The control objective of the MSC is to keep the stator voltage stable and achieve maximum power point tracking (MPPT). Keeping stator voltage stable can prevent stator overvoltage caused by generator overspeed. The control block diagram of the MSC is shown in Figure 1b. Power signal feedback control is adopted for MPPT of wind turbines. P_{ref} is given by the MPPT module. Calculating the corresponding maximum power value on the maximum power curve is based on the measured actual speed of the wind turbine. This maximum power value is P_{ref} .

3.2. BC Control

A BC is a protective device installed on the DC bus. It consists of DC chopper circuit and a DC resistor, as shown in Figure 1c. When the DC-link voltage exceeds a certain threshold, the circuit conducts and releases the surplus energy to keep the voltage stable [30].

There are many control methods for a braking chopper. The method of hysteresis comparison is shown in Figure 2a. This method has a simple control, but it causes excessive fluctuation of DC-link voltage and the DC-link voltage waveform is not smooth enough. Figure 2b shows that the duty cycle can be calculated using Equation (9). But in this method, it is difficult to control V_{dc} at the desired value. The method of generating duty cycle with a PI controller is shown in Figure 2c. However, the DC-link voltage has a significant overshoot in the initial stage of the fault due to the delay of the PI controller [31]. To solve this problem, a proportional integral derivative (PID) controller is adopted to replace the PI controller, which eliminates the overshoot in the initial stage of the fault.

$$m = R \frac{P_{gen} - P_{grid} - P_{ESS}}{V_{dc}^2} \tag{9}$$

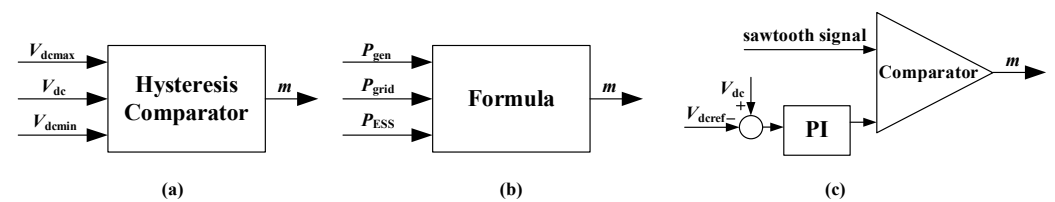


Figure 2. Control methods of a braking chopper: (a) hysteresis comparison; (b) power calculation; (c) PI control.

3.3. GSC Control

The control objective of the GSC is to keep the DC-link voltage stable. The reference value of reactive current is set to zero so that more active power can be transmitted to the grid during normal operation. The control block diagram of the GSC is shown in Figure 1d.

4. Proposed Nonlinear Robust Current Feedforward Control Based on an NLESO and GFTSMC

4.1. The Basic Principle of Current Feedforward Control

The generation side is equivalent to a DC load, and the structure of the GSC can be regarded as an AC/DC converter. The topology of it is shown in Figure 3. In Figure 3, e_a ,

e_b , and e_c are the voltage of the AC system; i_a , i_b , and i_c are the current of the AC system; v_a , v_b , and v_c are the voltage of the AC/DC converter; C is DC-link capacitance, i_o is the output current of the AC/DC converter, i_c is the capacitance current, i_{load} is the load current, V_{dc} is the DC-link voltage.

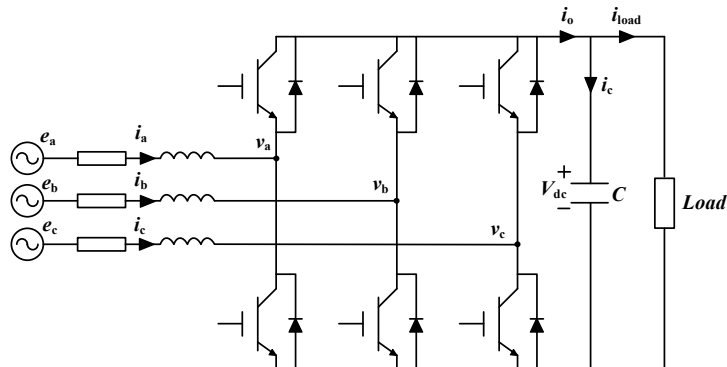


Figure 3. Topology of a grid side converter.

DC-link voltage control usually adopts a double closed-loop control composed of a voltage outer loop and a current inner loop. The block diagram of double closed-loop control is shown in Figure 4. G_v and G_i are the transfer function of voltage loop and current loop. V_{dcref} is the reference value of the DC-link voltage.

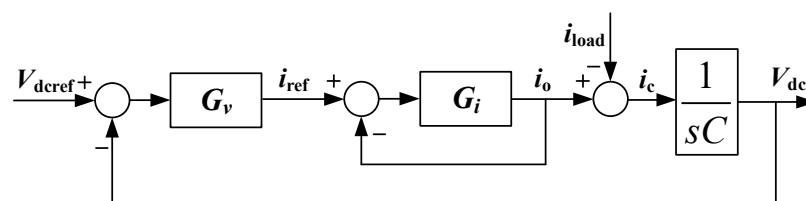


Figure 4. Block diagram of double closed-loop control.

According to this control block diagram, the expression of DC-link voltage is given as:

$$V_{dc}(s) = \frac{G_v(s)G_i(s)}{G_v(s)G_i(s) + G_i(s)sC + sC} V_{dcref}(s) - \frac{1 + G_i(s)}{G_v(s)G_i(s) + G_i(s)sC + sC} i_{load}(s) \quad (10)$$

From the above equation, it can be observed that the value of DC-link voltage is determined by two factors: the reference value of DC-link voltage and the load current. The load current always affects the reference value of the current after affecting the DC-link voltage, resulting in a large ripple of the DC-link voltage. This effect can be eliminated by current feedforward control. The double closed-loop control block diagram with current feedforward control is shown in Figure 5.

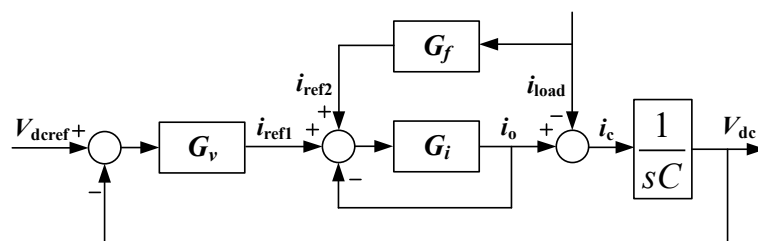


Figure 5. Double closed-loop control block diagram with current feedforward control.

According to the above figure, the DC-link voltage after adding current feedforward control is given as:

$$V_{dc}(s) = \frac{G_v(s)G_i(s)}{G_v(s)G_i(s) + G_i(s)sC + sC}V_{dcref}(s) + \frac{G_f(s)G_i(s) - G_i(s) - 1}{G_v(s)G_i(s) + G_i(s)sC + sC}i_{load}(s) \quad (11)$$

In order to eliminate the influence of load current, the coefficient of load current is set to zero. The transfer function of the feedforward control link is given as:

$$G_f(s) = \frac{1 + G_i(s)}{G_i(s)} \quad (12)$$

Due to the inherent delay of the PI controller, current feedforward control cannot fully eliminate the impact of load current.

4.2. Proposed Nonlinear Robust Current Feedforward Control

In actual operation, a PMSG wind power system is subjected to many external disturbances, resulting in the instability of DC-link voltage. Therefore, an NLESO and GFTSMC are used to design feedforward control in order to achieve the rapid stability of DC-link voltage. NLESO estimates the external disturbances of the system and compensates for the control law. Meanwhile, GFTSMC improves the system’s response speed.

From Figure 3, the following Equation (13) can be obtained by the Kirchhoff current law (KCL):

$$C \frac{dV_{dc}}{dt} = i_o - i_{load} \quad (13)$$

From Figure 5, the following Equation (14) can be obtained:

$$i_{ref2} = G_f(s)i_{load} = \frac{1 + G_i(s)}{G_i(s)}i_{load} \quad (14)$$

PI control is used for the current loop. The transfer function of it is given as Equation (15).

$$G_i(s) = K(1 + \frac{1}{sT}) \quad (15)$$

The following equation can be obtained from Equations (13)–(15):

$$\Delta \ddot{V}_{dc} = \frac{1}{C}i_o + \frac{K}{C(KT + T)}(Ti_{ref2} - i_{load}) - \frac{K}{C(KT + T)}i_{ref2} \quad (16)$$

where, K and T are the current loop parameters of the PI controller, ΔV_{dc} is the error of DC-link voltage.

Let

$$\begin{cases} x = \Delta V_{dc} \\ w(t) = \frac{1}{C}i_o + \frac{K}{C(KT+T)}(Ti_{ref2} - i_{load}) \\ b = -\frac{K}{C(KT+T)} \\ u(t) = i_{ref2} \end{cases} \quad (17)$$

Then, Equation (15) can be expressed as:

$$\begin{cases} \dot{x}_1 = x_2 \\ \dot{x}_2 = w(t) + bu(t) \end{cases} \quad (18)$$

Therefore, the system is a second-order system. An NLESO is designed to estimate the system state and external disturbance $\omega(t)$. The third-order NLESO is designed as:

$$\begin{cases} \dot{z}_1 = z_2 - \frac{k_1}{g'(z_1-x_1)}g(z_1-x_1) \\ \dot{z}_2 = z_3 - \frac{k_2}{g'(z_1-x_1)}g(z_1-x_1) + bu(t) \\ \dot{z}_3 = -\frac{k_3}{g'(z_1-x_1)}g(z_1-x_1) \end{cases} \tag{19}$$

where, z_1 and z_2 are the estimates of system states x_1 and x_2 , and z_3 is the estimate of external disturbance $\omega(t)$. The parameters k_1, k_2 , and k_3 are determined based on the dynamic parameter determination method. By selecting appropriate third-order polynomial poles, the eigenvalues of the system compensation matrix are located in the left half plane, ensuring the stability of the system under bounded conditions. $b = -K/(KCT + CT)$ is a constant related to the system.

The nonlinear function $g(z)$ is selected as:

$$g(z) = fal(z, \alpha, \delta) = \begin{cases} |z|^\alpha sign(z), & |z| \geq \delta \\ \frac{z}{\delta^{1-\alpha}}, & |z| < \delta \end{cases} \tag{20}$$

where, $\alpha = 0.5$ and $\delta = 0.01$.

The sliding mode surface is designed as:

$$s = z_2 + \alpha z_1 + \beta z_1^{q/p} \tag{21}$$

where, p and q are positive odd numbers, and $q < p$.

The control law is set as:

$$u(t) = -\frac{1}{b}(z_3 + \alpha z_2 + \beta \frac{q}{p} z_1^{(q/p-1)} \dot{z}_1 + \phi s + \gamma s^{q/p} - \frac{\alpha k_1 g(z_1-x_1)}{g'(z_1-x_1)} - \frac{k_2 g(z_1-x_1)}{g'(z_1-x_1)}) \tag{22}$$

where, ϕ and γ are constants. $\phi, \gamma > 0$.

Based on the above analysis, the control block diagram of nonlinear robust current feedforward control is shown in Figure 6. Nonlinear robust current feedforward control uses DC-link voltage as the input signal, eliminating the requirement for current measurement. In practical applications, the number of current transformers and cost is reduced.

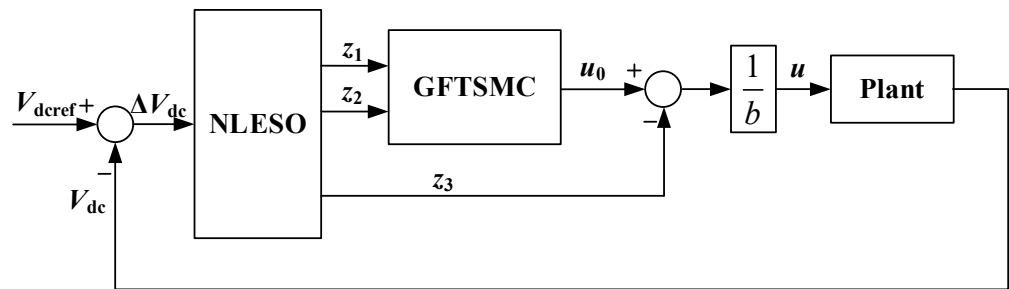


Figure 6. Control block diagram of nonlinear robust current feedforward control.

After adding the proposed control, the control block diagram of the GSC is shown in Figure 7.

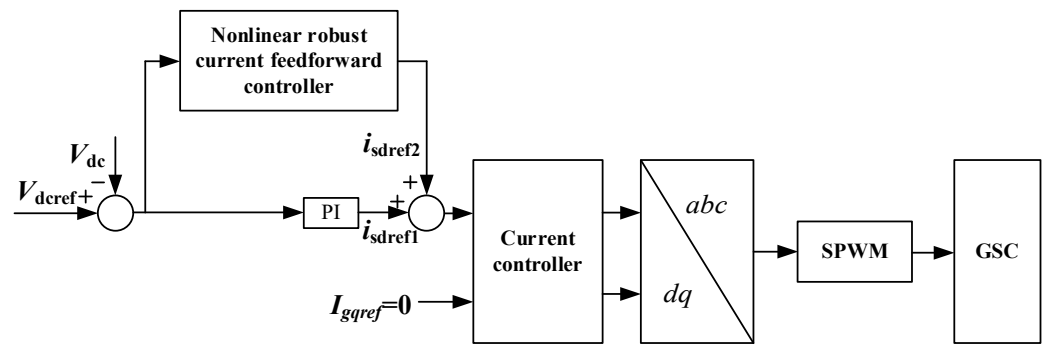


Figure 7. Control block diagram of the GSC with the proposed control.

4.3. Stability Analysis

To prove the stability of the system, the Lyapunov function is selected as:

$$V = 0.5s^2 \tag{23}$$

The following Equation (24) can be obtained by Equation (21),

$$\dot{s} = \dot{z}_2 + \alpha \dot{z}_1 + \beta \frac{q}{p} z_1^{(q/p)-1} \dot{z}_1 \tag{24}$$

Replace Equation (24) by (19) and (22),

$$\dot{s} = -\phi s - \gamma s^{q/p} \tag{25}$$

By solving this differential equation, it can be obtained that the time for the system to reach the sliding mode surface along Equation (23) is:

$$t = \frac{p}{\phi(p-q)} \ln \frac{\phi[x_1(0)]^{p-q/p} + \gamma}{\gamma} \tag{26}$$

The system can reach the sliding mode surface in a finite time. Combining Equations (22) and (24),

$$\dot{V} = s\dot{s} = s(-\phi s - \gamma s^{q/p}) = -\phi s^2 - \gamma s^{(q+p)/p} \tag{27}$$

since $\phi, \gamma > 0$, and $(q + p)$ is an even number, $\dot{V} \leq 0$. The system is stable.

5. Simulation Results

A DIgSILENT simulation was performed for a PMSG wind power system. The parameters of the PMSG wind power system are listed in Table 1. Since the ZVRT duration is short, the wind speed can be regarded as constant.

Table 1. Parameters of the PMSG wind power system.

System Component	Parameters	Values
Turbine	Wind speed	11 m/s
	Blade radius	45 m
	Air density	1.225 kg/m ³
	Max. Power conv. coeff	0.48
	Rated turbine speed	17.3 rpm
Shaft	Moment of inertia	6.1 × 10 ⁶ kgm ²
	Shaft stiffness	8.3 × 10 ⁷ Nm/rad
	Shaft mutual damping	1.4 × 10 ⁶ Nms/rad

Table 1. *Cont.*

System Component	Parameters	Values
PMSG	Rated power	2.5 MW
	Rated voltage	690 V
BTB converter with BC	DC-link voltage	1200 V
	DC-link capacitance	0.023 F
	Braking chopper resistance	0.67 Ω
	$V_{dcref-BC}$	1.1 p.u.
Grid	PCC voltage	690 V
	Grid voltage	35 KV
	Grid frequency	50 Hz

The parameters of the nonlinear robust current feedforward controller are listed in Table 2.

Table 2. Parameters of the controller.

Controller Component	Parameters	Values
NLESO	k_1	100
	k_2	3750
	k_3	62,500
	b	−2900
GFTSMC	α	0.5
	β	0.1
	p	9
	q	5
	ϕ	2
	Γ	4

5.1. Verification of Proposed Nonlinear Robust Current Feedforward Control

To verify the validity of proposed nonlinear robust current feedforward control based on an NLESO and GFTSMC, an 80% three-phase grid fault is added at the PCC. The fault is added at 0.5 s, and the fault duration is 625 ms. The simulation time is 2 s. The MSC and BC adopt the control strategies shown in Figure 1b,c. The GSC adopts the control strategy shown in Figure 7. Select the appropriate fault parameters so that the PCC voltage is 0.2 p.u. during the fault.

DC-link voltage under conventional double closed-loop control and the proposed control is shown in Figure 8. As shown in the figure, the first minimum value of the DC link voltage is reduced from 0.923 p.u. to 0.975 p.u. under the proposed control and the first maximum is reduced from 1.026 p.u. to 0.999 p.u. The stability time also reduces by approximately 0.15 s. It is evident that the proposed control has a significant impact on reducing voltage fluctuations and improving system stability.

5.2. Performance of PMSG Wind Power System under a Zero Voltage Grid Fault

To observe the performance of the PMSG wind power system under a zero voltage three-phase short-circuit fault, the fault occurs at the PCC at 0.5 s, and the fault is cleared in 0.9 s. The performance of the PMSG wind power system is shown in Figure 9.

As shown in Figure 9a, the PCC voltage drops instantly to zero when the fault occurs. Meanwhile, the GSC is unable to supply active power to the grid due to the voltage drop. Therefore, the GSC active power also drops to zero, as shown in Figure 9f. However, the fluctuation in PMSG terminal voltage and MSC active power is not significant under the influence of the MSC control strategy. This means that the active power on the motor side is still maintained at around 1 p.u. There is a significant power difference between the motor side and the grid side. This energy is stored in the capacitor, causing an increase in the DC-link voltage. By consuming this surplus energy through the BC, the rise in DC-link voltage

is prevented. DC-link voltage is maintained around 1.1 p.u. during the fault, as shown in Figure 9b. The switch signal of the BC is shown in Figure 9c. When the signal is one, the BC is put into the circuit, causing a drop in the DC-link voltage; when the signal is zero, it is triggered and the DC-link voltage increases. After the fault ends, there is still significant fluctuation in the DC-link voltage under conventional double closed-loop control due to the disturbance of the BC. In comparison, the DC-link voltage quickly returned to normal values under the proposed nonlinear robust current feedforward control. The compensated GSC active current is shown in Figure 9g. The PCC voltage and GSC reactive power have also recovered to normal values. The entire zero voltage ride through process ends.

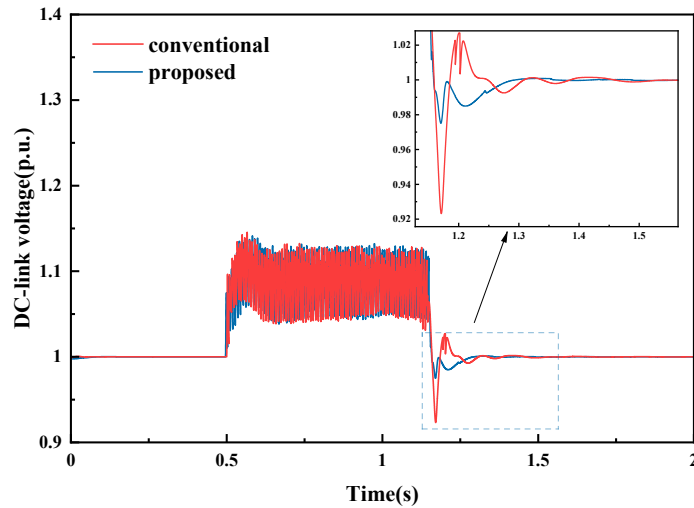


Figure 8. DC-link voltage under an 80% three-phase short circuit.

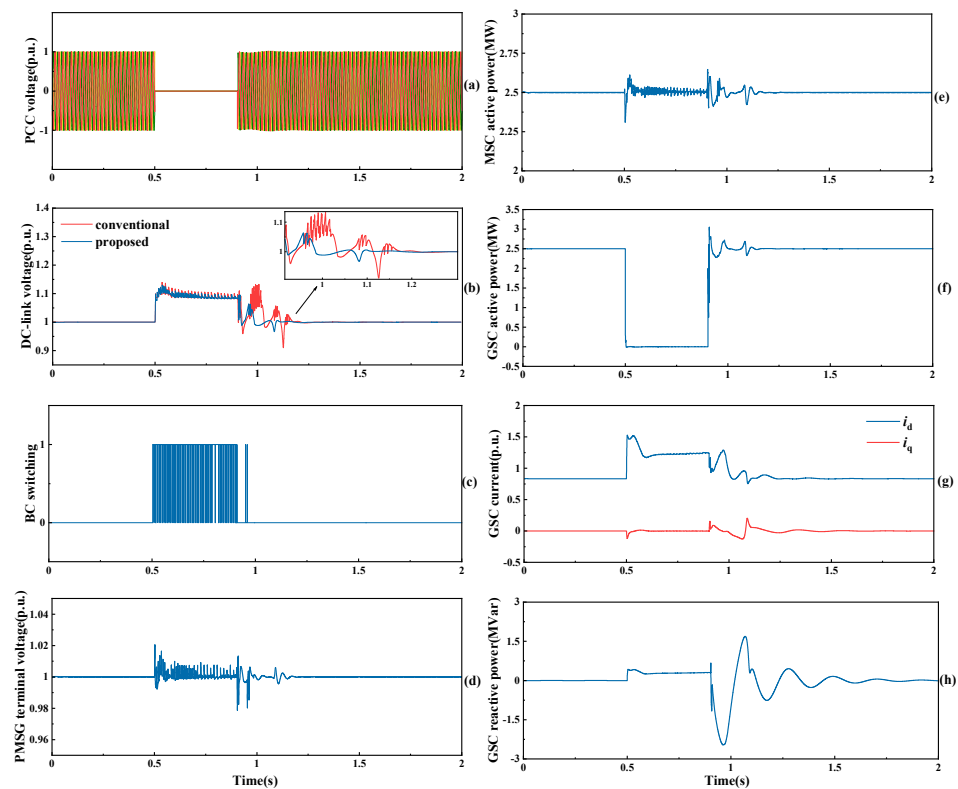


Figure 9. The performance of the PMSG wind power system under a zero voltage three-phase short-circuit fault: (a) PCC voltage; (b) DC-link voltage; (c) BC switching; (d) PMSG terminal voltage; (e) MSC active power; (f) GSC active power; (g) GSC current; (h) GSC reactive power.

Reactive power compensation is not considered in this paper. The mechanism of reactive power compensation and a control strategy combining reactive power compensation are being studied. In addition, there is still significant research value for BC control strategies based on advanced control theory.

6. Conclusions

This paper proposes a nonlinear robust current feedforward control for ZVRT of PMSG wind power systems. In the ZVRT scheme, the BC is utilized to dissipate surplus energy and current feedforward control is employed to reduce the fluctuation of DC-link voltage after the fault. An NLESO and GFTSMC are used to design the current feedforward control, which realizes the rapid stabilization of DC-link voltage. The main findings and contributions of this paper can be summarized as follows:

1. Simulation results show that the proposed nonlinear robust current feedforward control has an excellent control effect on DC-link voltage. This is specifically reflected in reducing the DC-link voltage fluctuation and recovery time after the fault.
2. This scheme realizes ZVRT with a high performance. DC-link voltage is kept within a safe range during the grid fault. All indicators are within normal values.
3. The NLESO and GFTSMC change the current feedforward control into a nonlinear robust current feedforward control by utilizing the DC-link voltage as the input signal. This reduces the number of current transformers and saves cost.

Author Contributions: Z.K. proposed current feedforward control based on an NLESO and GFTSMC; J.L. performed the modeling and simulation and wrote the manuscript. All authors have read and agreed to the published version of the manuscript.

Funding: This research was funded by the National Natural Science Foundation of China, grant number 52241702.

Data Availability Statement: Not applicable.

Conflicts of Interest: The authors declare no conflict of interest.

References

1. Nasiri, M.; Milimonfared, J.; Fathi, S.H. A review of low-voltage ride-through enhancement methods for permanent magnet synchronous generator-based wind turbines. *Renew. Sustain. Energy Rev.* **2015**, *47*, 399–415. [[CrossRef](#)]
2. Jahanpour-Dehkordi, M.; Vaez-Zadeh, S.; Mohammadi, J. Development of a Combined Control System to Improve the Performance of a PMSG-Based Wind Energy Conversion System under Normal and Grid Fault Conditions. *IEEE Trans. Energy Convers.* **2019**, *34*, 1287–1295. [[CrossRef](#)]
3. Zhou, A.; Li, Y.W.; Mohamed, Y. Mechanical Stress Comparison of PMSG Wind Turbine LVRT Methods. *IEEE Trans. Energy Convers.* **2021**, *36*, 682–692. [[CrossRef](#)]
4. Kim, K.; Jeung, Y.; Lee, D.; Kim, H. LVRT Scheme of PMSG Wind Power Systems Based on Feedback Linearization. *IEEE Trans. Power Electron.* **2012**, *27*, 2376–2384. [[CrossRef](#)]
5. Al-Shetwi, A.Q.; Hannan, M.A.; Jern, K.P.; Mansur, M.; Mahlia, T.M.I. Grid-connected renewable energy sources: Review of the recent integration requirements and control methods. *J. Clean. Prod.* **2020**, *253*, 119831. [[CrossRef](#)]
6. Qin, K.; Wang, S.; Kang, Z. Research on Zero-Voltage Ride through Control Strategy of Doubly Fed Wind Turbine. *Energies* **2021**, *14*, 2287. [[CrossRef](#)]
7. Ibrahim, R.A.; Hamad, M.S.; Dessouky, Y.G.; Williams, B.W. A review on recent low voltage ride-through solutions for PMSG wind turbine. In Proceedings of the International Symposium on Power Electronics Power Electronics, Electrical Drives, Automation and Motion, Sorrento, Italy, 20–22 June 2012; pp. 265–270.
8. Wang, J.; Ben, Y.; Zhang, J.; Feng, H. Low voltage ride-through control strategy for a wind turbine with permanent magnet synchronous generator based on operating simultaneously of rotor energy storage and a discharging resistance. *Energy Rep.* **2022**, *8*, 5861–5870. [[CrossRef](#)]
9. Nasiri, M.; Arzani, A. Robust control scheme for the braking chopper of PMSG-based wind turbines—A comparative assessment. *Int. J. Electr. Power Energy Syst.* **2021**, *134*, 107322. [[CrossRef](#)]
10. Sakipour, R.; Abdi, H. Voltage stability improvement of wind farms by self-correcting static volt-ampere reactive compensator and energy storage. *Int. J. Electr. Power Energy Syst.* **2022**, *140*, 108082. [[CrossRef](#)]
11. Huang, C.; Xiao, X.Y.; Zheng, Z.; Wang, Y. Cooperative Control of SFCL and SMES for Protecting PMSG-Based WTGs under Grid Faults. *IEEE Trans. Appl. Supercond.* **2019**, *29*, 1–6. [[CrossRef](#)]

12. Sathya, E.; Maruthupandi, P. Enhancement of Low Voltage Ride through Capability for PMSG Based Wind Energy Conversion System with Super Capacitor. In Proceedings of the 2018 4th International Conference on Electrical Energy Systems (ICEES), Chennai, India, 7–9 February 2018; pp. 57–60.
13. Chen, L.; Chen, H.; Yang, J.; Zhu, L.; Tang, Y.; Koh, L.H.; Xu, Y.; Zhang, C.; Liao, Y.; Ren, L. Comparison of Superconducting Fault Current Limiter and Dynamic Voltage Restorer for LVRT Improvement of High Penetration Microgrid. *IEEE Trans. Appl. Supercond.* **2017**, *27*, 1–7. [[CrossRef](#)]
14. Jin, J.X.; Yang, R.H.; Zhang, R.T.; Fan, Y.J.; Xie, Q.; Chen, X.Y. Combined low voltage ride through and power smoothing control for DFIG/PMSG hybrid wind energy conversion system employing a SMES-based AC-DC unified power quality conditioner. *Int. J. Electr. Power Energy Syst.* **2021**, *128*, 106733. [[CrossRef](#)]
15. Benali, A.; Khiaat, M.; Allaoui, T.; Denai, M. Power Quality Improvement and Low Voltage Ride through Capability in Hybrid Wind-PV Farms Grid-Connected Using Dynamic Voltage Restorer. *IEEE Access* **2018**, *6*, 68634–68648. [[CrossRef](#)]
16. Feyzi, M.; Roozbehani, S.; Liasi, S.G. Low Voltage Ride through Improvement of Machine Side and Grid Side Converters of PMSG-Wind Turbine Based on SMC. In Proceedings of the 2022 13th Power Electronics, Drive Systems, and Technologies Conference (PEDSTC), Tehran, Iran, 1–3 February 2022; pp. 251–257.
17. Calle-Prado, A.; Alepuz, S.; Bordonau, J.; Nicolas-Apruzzese, J.; Cortés, P.; Rodriguez, J. Model Predictive Current Control of Grid-Connected Neutral-Point-Clamped Converters to Meet Low-Voltage Ride-through Requirements. *IEEE Trans. Ind. Electron.* **2015**, *62*, 1503–1514. [[CrossRef](#)]
18. Alhejji, A.; Bouzid, Y. Robust Adaptive PI Controller of Low Voltage Ride-through for PMSG-Based Wind Turbine. In Proceedings of the 2019 6th International Conference on Control, Decision and Information Technologies (CoDIT), Paris, France, 23–26 April 2019; pp. 1233–1237.
19. Uehara, A.; Pratap, A.; Goya, T.; Senjyu, T.; Yona, A.; Urasaki, N.; Funabashi, T. A Coordinated Control Method to Smooth Wind Power Fluctuations of a PMSG-Based WECS. *IEEE Trans. Energy Convers.* **2011**, *26*, 550–558. [[CrossRef](#)]
20. Xing, P.; Fu, L.; Wang, G.; Wang, Y.; Zhang, Y. A compositive control method of low-voltage ride through for PMSG-based wind turbine generator system. *IET Gener. Transm. Distrib.* **2018**, *12*, 117–125. [[CrossRef](#)]
21. Wang, M.; Tian, Y.; Feng, X.; Chen, G. A hybrid LVRT control scheme for PMSG wind power system. In Proceedings of the 7th International Power Electronics and Motion Control Conference, Harbin, China, 2–5 June 2012; pp. 1173–1177.
22. Junejo, A.K.; Xu, W.; Mu, C.; Ismail, M.M.; Liu, Y. Adaptive Speed Control of PMSM Drive System Based a New Sliding-Mode Reaching Law. *IEEE Trans. Power Electron.* **2020**, *35*, 12110–12121. [[CrossRef](#)]
23. Xu, W.; Junejo, A.K.; Liu, Y.; Hussien, M.G.; Zhu, J. An Efficient Antidisturbance Sliding-Mode Speed Control Method for PMSM Drive Systems. *IEEE Trans. Power Electron.* **2021**, *36*, 6879–6891. [[CrossRef](#)]
24. Haque, M.E.; Negnevitsky, M.; Muttaqi, K.M. A Novel Control Strategy for a Variable-Speed Wind Turbine with a Permanent-Magnet Synchronous Generator. *IEEE Trans. Ind. Appl.* **2010**, *46*, 331–339. [[CrossRef](#)]
25. Ghany, A.A.; Shehata, E.G.; Elsayed, A.-H.M.; Mohamed, Y.S.; Haes Alhelou, H.; Siano, P.; Diab, A.A.Z. Novel Switching Frequency FCS-MPC of PMSG for Grid-Connected Wind Energy Conversion System with Coordinated Low Voltage Ride through. *Electronics* **2021**, *10*, 492. [[CrossRef](#)]
26. Babaghorbani, B.; Beheshti, M.T.; Talebi, H.A. A Lyapunov-based model predictive control strategy in a permanent magnet synchronous generator wind turbine. *Int. J. Electr. Power Energy Syst.* **2021**, *130*, 106972. [[CrossRef](#)]
27. Nasiri, M.; Mohammadi, R. Peak Current Limitation for Grid Side Inverter by Limited Active Power in PMSG-Based Wind Turbines during Different Grid Faults. *IEEE Trans. Sustain. Energy* **2017**, *8*, 3–12. [[CrossRef](#)]
28. Kim, C.; Kim, W. Enhanced Low-Voltage Ride-through Coordinated Control for PMSG Wind Turbines and Energy Storage Systems Considering Pitch and Inertia Response. *IEEE Access* **2020**, *8*, 212557–212567. [[CrossRef](#)]
29. Huang, C.; Zheng, Z.; Xiao, X.; Chen, X. Enhancing low-voltage ride-through capability of PMSG based on cost-effective fault current limiter and modified WTG control. *Electr. Power Syst. Res.* **2020**, *185*, 106358. [[CrossRef](#)]
30. Pannell, G.; Zahawi, B.; Atkinson, D.J.; Missailidis, P. Evaluation of the Performance of a DC-Link Brake Chopper as a DFIG Low-Voltage Fault-Ride-through Device. *IEEE Trans. Energy Convers.* **2013**, *28*, 535–542. [[CrossRef](#)]
31. Orlando, N.A.; Liserre, M.; Mastromauro, R.A.; Dell, A. A Survey of Control Issues in PMSG-Based Small Wind-Turbine Systems. *IEEE Trans. Ind. Inform.* **2013**, *9*, 1211–1221. [[CrossRef](#)]

Disclaimer/Publisher’s Note: The statements, opinions and data contained in all publications are solely those of the individual author(s) and contributor(s) and not of MDPI and/or the editor(s). MDPI and/or the editor(s) disclaim responsibility for any injury to people or property resulting from any ideas, methods, instructions or products referred to in the content.